Simulation Study of Neutral Tungsten Emissions for Fusion Applications

Ritu DEY[1)*†], Ayushi AGRAWAL[2)†], Reetesh KUMAR GANGWAR[1)], Deepti SHARMA[3)], Rajesh SRIVASTAVA[2)], Malay B. CHOWDHURI[3)], Joydeep GHOSH[3,4)]

[1)] *Department of Physics, Indian Institute of Technology Tirupati, Yerpedu 517619, India*
[2)] *Department of Physics, Indian Institute of Technology Roorkee, Roorkee 247667, India*
[3)] *Institute for Plasma Research, Gandhinagar 382428, India*
[4)] *Homi Bhabha National Institute, Training School Complex, Anushakti Nagar, Mumbai 400094, India*

(Received 29 August 2025 / Accepted 25 January 2026)

The article reports electron-impact excitation cross-sections and rate coefficients for neutral tungsten for three transitions (400.87, 429.46, and 430.21 nm) using the relativistic distorted wave approach within the flexible atomic code. Some of these lines are also observed in tokamak plasma. Cross-sections are computed for incident electron energy up to 30 keV. The energy levels in flexible atomic code were corrected to match the NIST database. The electron impact excitation rate coefficients are also provided.

Keywords: tungsten, FAC, cross-section, rate-coefficient

DOI: 10.1585/pfr.21.2403022

1. Introduction

Tungsten is a highly valuable material for magnetic confinement devices due to its low tritium retention, low erosion rate, and high melting point. These properties make it an ideal choice for critical components in fusion reactors. As a result, tungsten is used in the construction of the ITER first wall and divertor plates [1] to handle the high heat fluxes. Similarly, the upgrade version of EAST used a ITER-like tungsten monoblock divertor configuration [2, 3]. Moreover, WEST is a superconducting, actively cooled, full tungsten (W) tokamak [4]. Previously, there were many studies involving erosion due to tungsten [5]. For example, in the divertor of the ASDEX-Upgrade tokamak, erosion properties are investigated by observing the W I emission line at 400.9 nm [5]. It is found that the sputtering yield is in the order of 10^{-4} atoms/ion for typical divertor plasma conditions. JET used tungsten on the divertors [6] to handle the wall materials issues that are critical for the fusion devices. The usage of tungsten material makes it abundant in fusion devices, and it presents as an impurity material. Due to a large radial variation of electron temperature in tokamak devices, various charged states of tungsten along with the neutral can exist inside the tokamak. Over the years, spectroscopic investigations/diagnostics have been carried out to study the W emissions [7] to determine the erosion rate. Various theoretical approaches are used to calculate the energy levels, radiative transition probabilities, and ionization/excitation cross sections, which support the spectroscopic diagnostics results. The various approaches applied worldwide for the above purpose are relativistic distorted wave approximation (RDW) [8], relativistic Hartree-Fock method [9], multi-configuration Dirac-Fock method (MCDF) [10], binary encounter Bethe Model [11], etc. The well-known codes in which these methods are implemented to calculate various atomic structures are Cowan [12, 13], flexible atomic code (FAC) [14], DARC [15], GRASP [16] and MDFGME [17]. Very recently, Duck-Hee Kwon and Paul Indelicato [18] reported MCDF calculations to obtain radiative electron-impact transition rates for neutral tungsten. They have reported electron impact excitation rate-coefficients for visible transition wavelengths of neutral W of 400.87, 488.69, 498.26, and 522.47 nm for incident electron energy up to 30 eV. They found that the accuracies for electron impact excitation (EIE) cross-sections are challenging, and more experimental and theoretical investigations are necessary to evaluate the neutral W emissions. To address this issue, in the present manuscript, the electron impact excitation cross sections are calculated by using the relativistic distorted wave approximation within the FAC [14] code for the neutral W atom up to an incident electron energy of 30 keV. It is worth mentioning that the FAC can calculate configuration-interaction with many configurations without a convergence problem compared with the MCDF calculation. It is to be noted that these W I emission lines are observed in laser induced breakdown spectrsocopy (LIBS)

**Corresponding author's e-mail: ritu.dey@iittp.ac.in*
† Contributed equally
This article is based on the presentation at the Joint Conference of the 22nd International Conference on Atomic Processes in Plasmas (APiP 2025) and 1st NIFS Conference on Atomic and Molecular Processes in Plasmas.

experiments [19]. To the best of our knowledge, the results reported here are presented for the first time, except for those at the 400.87 nm wavelength. Furthermore, the cross-sections are integrated over electron energy space to obtain the Maxwellian-averaged EIE rate coefficients. The paper is organized as follows: Section 2 describes the brief theory for calculating the cross-sections and rate coefficients within the RDW approximation. Section 3 contains the results. A concluding remark is given in Sec. 4.

2. Theory

Flexible atomic code (FAC) [14] Version 1.1.5 is used to simulate the EIE cross-sections. The radial wavefunctions for single-electron orbitals are obtained with a self-consistent field method based on the Dirac equations. The Dirac-Coulomb Hamiltonian is diagonalized to obtain energy levels and atomic state wavefunctions. This code used the RDW approximation to determine the collision strength for EIE process for neutral W. The collision strength (Ω_{01}) is expressed as,

$$\Omega_{01} = 2\sum_{k}\sum_{\alpha_0\alpha_1\beta_0\beta_1} Q^k(\alpha_0\alpha_1;\beta_0\beta_1) \left\langle\Psi_0\|Z^k(\alpha_0,\alpha_1)\|\Psi_1\right\rangle\left\langle\Psi_0\|Z^k(\beta_0,\beta_1)\|\Psi_1\right\rangle, \quad (1)$$

where,

$$Q^k(\alpha_0\alpha_1;\beta_0\beta_1) = \sum_{\kappa_0,\kappa_1}[k]^{-1} P^k(\kappa_0\kappa_1;\alpha_0\alpha_1)P^k(\kappa_0\kappa_1;\beta_0\beta_1). \quad (2)$$

κ_0, κ_1 are the relativistic angular quantum numbers of the incident and the scattered electrons, respectively. Ψ_0 and Ψ_1 are the wave-functions of the initial and final state, respectively. $Z^k(\alpha_0,\alpha_1)$ and $Z^k(\beta_0,\beta_1)$ are the tensor operators. α_0, α_1, β_0 and β_1 are the orbitals of the electron. The radial integral $Q^k(\alpha_0\alpha_1;\beta_0\beta_1)$ contains (P^k) which is expressed as:

$$P^k(\kappa_0\kappa_1;\alpha_0\alpha_1) = X^k(\alpha_0\kappa_0;\alpha_1\kappa_1) + \sum_t (-1)^{k+t}[k] \times \begin{Bmatrix} J_{\alpha_0} & J_1 & t \\ j_0 & j_{\alpha_1} & k \end{Bmatrix} X^t(\alpha_0\kappa_0;\kappa_1\alpha_1). \quad (3)$$

X^k is the two electron Slater integral and k is the multipolarity. The total EIE cross-section is expressed in terms of collision strength as (in atomic unit) follows:

$$\sigma_{01} = \frac{\pi}{k_0^2 g_0}\Omega_{01}. \quad (4)$$

Because the RDW theory is perturbative, its accuracy near threshold energies is limited. Therefore, low-energy corrections up to approximately two to three times the excitation threshold are required. The corrected cross section, expressed as a function of the projectile electron energy, is given below [20].

$$\sigma_{01[corrected]} = [1 - (E_{threshold}/E)^{\frac{1}{2}}]\sigma_{01}, \quad (5)$$

where E is the electron energy and $E_{threshold}$ is the threshold energy for the excitation. The similar equation is applied to find out the electron impact excitation cross-sections and rate coefficients using fully relativistic distorted wave approach of cesium atom [21].

The electron-impact excitation cross-section is integrated over the Maxwellian electron energy space and then the rate coefficient is expressed as:

$$R_{ij} = 2\sqrt{\left(\frac{1}{\pi m_e}\right)}(K_B T_e)^{-3/2} \int_{\epsilon}^{\infty} E\sigma_{ij}(E) exp\left(-\frac{E}{K_B T_e}\right)dE, \quad (6)$$

where, K_B is the Boltzmann coefficient and m_e, T_e are the mass and temperature of the electron, respectively. ϵ is the threshold energy for the particular transition.

3. Results and Discussion

In the present work, FAC is parallelized and executed using 32 CPU cores on ANTYA, an IPR LINUX cluster, to calculate the EIE cross-sections and rate coefficients. It is worth mentioning that the cross-sections and rate coefficients calculated for the particular transitions in the visible range, which are often measured in plasma diagnostics [4, 6], are found in various tokamaks. It is also observed by the LIBS experiment [19]. Neutral tungsten atom which has a total of 74 electrons and the ground state configuration is [Xe] $4f^{14}$ $5d^4 6s^2$ ($^5D_0$). The atomic structure of neutral tungsten (W I) contains partially filled 5d subshells and due to this the complexity arises in theoretical modelling to investigate the fine-structure spectrum. A total of 43,556 fine-structure-resolved energy levels are considered, corresponding to the excited level configurations. The configurations that are taken for the present calculations are as follows: $5p^6 5d^4 6[s^2,p^2,d^2]$, $5p^6 5d^4 6s6[p,d]$, $5p^6 5d^4 6s7[s,p,d,f]$, $5p^6 5d^6$, $5p^6 5d^3 6s6[p^2,d^2]$, $5p^6 5d^2 6s^2 6p^2$, $5p^6 5d^2 6s^2 6d^2$, $5p^6 5d^4 7s^2$, $5p^6 5d^3 6s7s^2$, $5p^6 5d^2 6s^2 7s^2$, $5p^6 5d^3 6s^2 6d$, $5p^6 5d^5 7s$, $5p^6 5d^3 6s^2 7s$, $5p^6 5d^5 6[s,p,d]$, $5p^6 5d^3 6s^2 6p$, $5p^6 5d^3 6p^3$, $5p^6 5d^2 6s6p^3$, $5p^6 5d^4 6s8[s,p,d,f]$, $5p^6 5d^4 6s9[s,p,d,f]$, $5p^6 5d^3 6s^2 7p$, $5p^6 5d^5 7p$, $5p^6 5d^4 6s5f$, $5p^6 5d^5 5f$, $5p^6 5d^3 6d^3$, $5p^6 5d6s^2 6d^3$, $5p^5 5d^5 6s6p$, $5p^5 5d^6 6p$, $5p^5 5d^6 6s$, $5p^5 5d^7$, $5p^5 5d^5 6s^2$, $5p^5 5d^5 6s7[s,p,d]$, $5p^5 5d^5 6s8[s,p,d]$, $5p^5 5d^6 6p$, $5p^5 5d^4 6s^2 6p$, $5p^4 5d^6 6s^2$, $5p^4 5d^7 6s$, $5p^4 5d^8$, $5p^4 5d^6 6s6p$, $5p^4 5d^7 6p$, $5p^4 5d^5 6s^2 6p$, $5p^4 5d^6 6s^2$, $5p^4 5d^7 6s$, $5p^4 5d^8$.

Table 1 presents the upper-state configurations and excitation energies (E_k) of neutral tungsten (W I) corresponding to the 400.87, 429.46, and 430.21 nm transitions. The results obtained from the FAC simulation are compared with data from the NIST database [22] as well as calculations using the GRASP [23] and MDFGME [18] codes. The results from various MDFGME calculations, depending on the configurations included in the configuration interaction (CI), are denoted as $MDFGME_1$, $MDFGME_2$, and $MDFGME_3$. Specifically, the $MDFGME_1$ results correspond to calculations performed using the MCDF method, incorporating configurations 1–10 (even

Table 1. Configurations and upper energy levels of W I transitions from FAC, GRASP [23], MDFGME [18] and the NIST [22] recommended values based on experiment.

Wavel. (nm)	Config. level	E_k FAC (eV)	E_k NIST (eV)	E_k GRASP (eV)	E_k $MDFGME_1$ (eV)	E_k $MDFGME_2$ (eV)	E_k $MDFGME_3$ (eV)
400.87	$5d^5(^6S)6p\ (^7P^0_4)$	4.458	3.457	2.980	3.114	3.608	3.566
429.46	$5d^5(^6S)6p\ (^7P^0_2)$	3.980	3.252	2.971	2.969	3.549	3.486
430.21	$5d^46s(^6D)6p\ (^7D^0_3)$	2.233	3.247	2.823	2.952	3.443	3.391

Table 2. Transition probabilities (A_{ij}) of W I transitions from FAC, GRASP [23], MDFGME [18] and the NIST [22] database.

Wavel. (nm)	A_{ij} FAC (s^{-1})	A_{ij} NIST (s^{-1})	A_{ij} GRASP (s^{-1})	A_{ij} $MDFGME_1$ (s^{-1})	A_{ij} $MDFGME_2$ (s^{-1})	A_{ij} $MDFGME_3$ (s^{-1})
400.87	6.82×10^7	1.63×10^7	1.14×10^7	2.54×10^7	2.34×10^7	2.41×10^7
429.46	3.08×10^7	1.24×10^7	3.17×10^7	2.45×10^7	2.14×10^7	2.37×10^7
430.21	2.76×10^6	3.60×10^6	4.54×10^6	9.06×10^6	8.68×10^6	8.11×10^6

Table 3. Oscillator strengths of W I transitions from FAC and the NIST database [22].

Wavel. (nm)	FAC	NIST
400.87	1.47	5.05×10^{-2}
429.46	4.27×10^{-1}	2.45×10^{-2}
430.21	5.35×10^{-2}	1.00×10^{-2}

parity) and 1–5 (odd parity) as listed in Tables 1 and 2 of Ref. [18], respectively. Meanwhile, $MDFGME_2$ and $MDFGME_3$ include additional CI effects. In particular, $MDFGME_2$ accounts for core-valence correlations, while $MDFGME_3$ incorporates both core-core and core-valence correlations. The energy levels of $5d^5(^6S)6p\ (^7P^o_2)$, $5d^5(^6S)6p\ (^7P^o_4)$, and $5d^46s(^6D)6p\ (^7D^o_3)$ differ from the NIST values by factors of approximately 1.2, 1.3, and 1.5, respectively. It is noted from Table 1 that the energy level corresponding to the $5d^5(^6S)6p\ (^7P^o_2)$, $5d^5(^6S)6p\ (^7P^o_4)$ agree within ~ 12% and 20% respectively, with the $MDFGME_2$ calculation using MCDF and additional CI methods with core-valence correlation. It is also observed that the energy levels obtained from the GRASP and MDFGME calculations exhibit deviations from the NIST database values. It is noticed that all three transitions are dipole allowed transitions and the FAC simulated transition probabilities (A_{ij}) are listed in Table 2. The table also includes transition probabilities from the NIST database [22] as well as calculations using the GRASP [23] and MDFGME [18] codes. These calculated probabilities show differences compared to the corresponding NIST values for the same wavelengths. The oscillator strengths calculated using FAC, together with those reported in the NIST database, are also presented in Table 3. The oscillator strengths differ from each other for all the three transitions considered. It is worth mentioning that further inclusion of the states there is no substantial improvement in the oscillator strengths and energy levels from the FAC simulation. The energy levels from FAC are corrected to match with the energy values from the NIST to calculate collision strengths for the above three transitions. Figure 1 displays the collision strength for

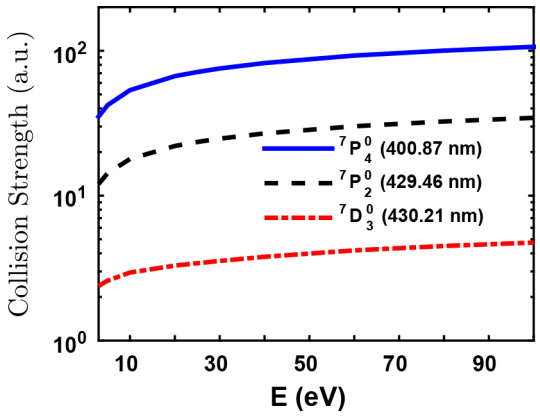

Fig. 1. Simulated EIE collison strengths for the excitation from $5d^5(^6S)6s\ (^7S_3)$ to $5d^5(^6S)6p\ (^7P^0_4)$ (blue-solid curve), $5d^5(^6S)6p\ (^7P^0_2)$ (black dashed curve) and $5d^46s(^6D)6p\ (^7D^0_3)$ (red dash-dotted curve), respectively.

the above three transitions listed in Table 1. Figure 1 shows the collision strengths for transitions from $5d^56s\ (^7S_3)$ to $5d^56p\ (^7P^o_4$ and $^7P^o_2)$, as well as from $5d^56s$ to $5d^46s6p\ (^7D^o_3)$, vary by approximately a factor of two over the incident electron energy range of 10–100 eV. The collision strength for the $5d^56s$ to $5d^46s6p\ (^7D^o_3$, 430.21 nm) transition shows a lower magnitude than for the other two transition wavelengths (400.87 and 429.46 nm) because the corresponding transition probability is significantly smaller. The upper level of the transition $5d^56s$ to $5d^46s6p$, is strongly configuration-mixed, with its wave function composed of about 54% $5d^46s6p$ and 14% $5d^56p$. Since an electric-dipole (E1) transition from the initial level $5d^56s$ connects most strongly to $5d^56p$ due to the same parent configuration, only the 14% component of the mixed state contributes to the dipole matrix element. This may be the reason why the collision strength is lower than the other two transitions. Furthermore, the EIE cross-sections that are related to collision strength through Eq. (4) are evaluated for all three transitions and plotted in Fig. 2. They follow the same pattern of decreasing with the incident electron energy. The cross-sections are simulated up to an incident electron

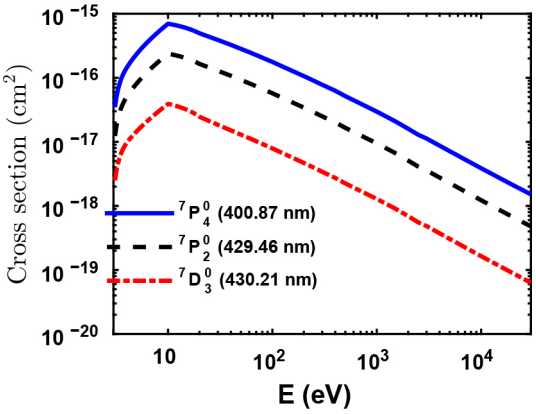

Fig. 2. Simulated EIE cross-sections for the excitation from $5d^5(^6S)6s$ ($^7S_3$) to $5d^5(^6S)6p$ ($^7P^0_4$) (blue-solid curve), $5d^5(^6S)6p$ ($^7P^0_2$) (black dashed curve) and $5d^46s(^6D)6p$ ($^7D^0_3$) (red dash-dotted curve), respectively.

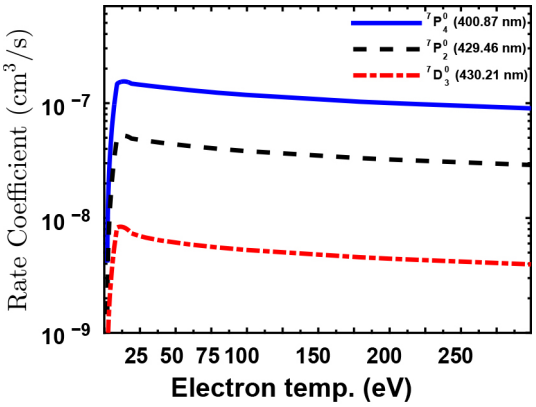

Fig. 3. Notations are similar to the Fig. 1, simulated EIE rate-coefficients for the neutral W.

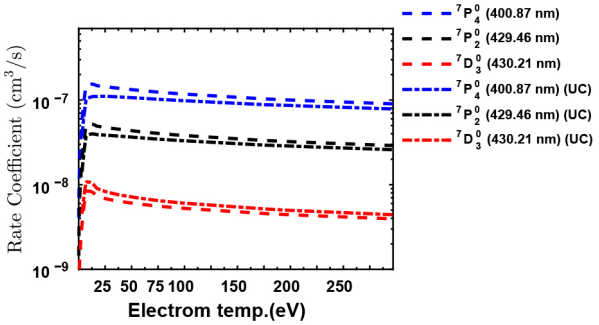

Fig. 4. Simulated EIE rate coefficients for the excitation from $5d^5(^6S)6s$ ($^7S_3$) to $5d^5(^6S)6p$ ($^7P^0_4$) (blue-dashed curve), $5d^5(^6S)6p$ ($^7P^0_2$) (black dashed curve) and $5d^46s(^6D)6p$ ($^7D^0_3$) (red dashed curve), respectively for corrected energy levels. The blue, black and red dash-dotted curves represent the FAC simulated EIE rate coefficients uncorrected energy levels.

energy of 30 keV. Near the threshold energy, the cross sections are corrected after using Eq. (5). The maximum magnitudes are 6.98×10^{-16}, 2.37×10^{-16}, and 3.91×10^{-17} cm^2 at an incident electron energy of ~ 10.0 eV for the transition wavelengths, 400.87, 429.46, and 431.21 nm, respectively. They fall ~ 500 times at an incident electron energy of 30 keV. Additionally, Fig. 3 depicts the EIE rate coefficients for the transition wavelengths of 400.87, 429.46, and 430.21 nm, respectively. The rate coefficients are obtained after averaging over the Maxwellian electron energy space using Eq. (6). The electron impact excitation rate coefficients for the transition wavelengths 400.87, 429.46, and 430.21 nm vary within a factor of ~ two times for the energy range 10–300 eV. It is worth mentioning that the EIE rate coefficients of W I reported by Kwon *et al*. [18] are for 400–522 nm range wavelengths and for incident electron energy up to 30 eV. The present simulated EIE rate coefficient for 400.87 nm transition wavelength is ~ 2.5 times higher than their Dirac-R matrix calculations for the energy range ~ 10 to 30 eV.

Finally, Fig. 4 illustrates the EIE rate coefficients for the above mentioned neutral W wavelengths, simulated with and without corrected excited energy levels. It is noticed that, the maximum deviation in EIE rate coefficients with uncorrected energy levels are maximum ~ 1.5 times for all the three transitions (($5d^5(^6S)6s$ ($^7S_3$) to - $5d^5(^6S)6p$ ($^7P^0_4$), - $5d^5(^6S)6p$ ($^7P^0_2$) and - $5d^46s(^6D)6p$ ($^7D^0_3$)) considered. It is hereby confirmed that energy level corrections are necessary to obtain the accurate collision strengths and cross sections for the neutral W.

4. Conclusion

The electron impact excitation cross-sections for W I are simulated with RDW approximation within the FAC code. The Maxwellian averaged rate coefficients are also presented. The wavelengths which are considered presently are, 400.87, 429.46, and 430.21 nm which correspond to transition from $5d^5(^6S)6s$ ($^7S_3$) to $5d^5(^6S)6p$ ($^7P^0_4$), $5d^5(^6S)6p$ ($^7P^0_2$) and $5d^46s(^6D)6p$ ($^7D^0_3$), respectively. The electron impact excitation rate coefficients for transitions in the visible range are presented, which will contribute significantly to spectroscopic diagnostics in fusion devices.

5. Acknowledgements

The authors, Ritu Dey, Reetesh Kumar Gangwar, Deepti Sharma, Rajesh Srivastava, and Joydeep Ghosh acknowledge the Board of Research in Nuclear Sciences (BRNS), DAE, Government of India, for supporting this work under research project grant (sanction no. 57/14/01/2023/12089). One of the author, Ritu Dey acknowledges Dr. Ankit Dhaka of the Institute for Plasma Research (IPR) for his assistance in running the parallelized FAC code on ANTYA, the IPR Linux Cluster. The simulation results presented in this study were obtained using ANTYA, the IPR Linux Cluster.

[1] R.A. Pitts *et al.*, Nucl. Mater. Energy **20**, 100696 (2019).
[2] C. Sang *et al.*, Nucl. Fusion **61**, 066004 (2021).
[3] Y. Wu *et al.*, Nucl. Mater. Energy **33**, 101297 (2022).
[4] J. Bucalossi *et al.*, Nucl. Fusion **64**, 112022 (2024).
[5] A. Thoma *et al.*, Plasma Phys. Control. Fusion **39**, 1487 (1997).

[6] G.F. Matthews *et al.*, Phys. Scr. **T128**, 137 (2007).
[7] I. Beigman *et al.*, Plasma Phys. Control. Fusion **49**, 1833 (2007).
[8] Priti *et al.*, Atoms **3**, 53 (2015).
[9] P. Quinet *et al.*, J. Phys. B, At. Mol. Opt. Phys. **44**, 1883 (2011).
[10] J.P. Desclaux, Comput. Phys. Commun. **9**, 31 (1975).
[11] Y.-K. Kim and M.E. Rudd, Phys. Rev. A **50**, 3954 (1994).
[12] R.D. Cowan, *The Theory of Atomic Structure and Spectra* (University of California Press, Berkeley, CA, USA, 1981).
[13] A. Kramida, Atoms **7**, 64 (2019).
[14] M.F. Gu, Can. J. Phys. **86**, 675 (2008).
[15] C. Ballance, Dirac atomic R-matrix code (2005).
[16] K. Dyall *et al.*, Comput. Phys. Commun. **55**, 425 (1989).
[17] P. Indelicato, MDFGME, a multiconfiguration Dirac-Fock and general matrix elements program (2024). https://www.lkb.upmc.fr/metrologysimplesystems/mdfgme-a-general-purpose-muticonnfiguration-dirac-foc-program/
[18] D.-H. Kwon and P. Indelicato, Eur. Phys. J. D. **78**, 86 (2024).
[19] B. Hegde *et al.*, private communication (2025).
[20] D. Wünderlich *et al.*, J. Quant. Spectrosc. Radiat. Transfer **149**, 360 (2014).
[21] Priti *et al.*, J. Quant. Spectrosc. Radiat. Transfer **187**, 426 (2017).
[22] A. Kramida *et al.*, NIST Database (ver. 5.12) (2024). https://physics.nist.gov/asd.
[23] R.T. Smyth *et al.*, Phys. Rev. A **97**, 052705 (2018).